Importance of Anode Microstructure in Modeling Solid Oxide Fuel Cells

Steven C. DeCaluwe,[a,*] Huayang Zhu,[b,**] Robert J. Kee,[b,**] and Gregory S. Jackson[a,**,z]

[a]*Department of Mechanical Engineering, University of Maryland, College Park, Maryland 20742, USA*
[b]*Engineering Division, Colorado School of Mines, Golden, Colorado 80401, USA*

A one-dimensional button-cell model is developed and applied to explore the influence of anode microstructure on solid oxide fuel cell (SOFC) performance. The model couples porous-media gas transport and elementary electrochemical kinetics within a porous Ni–yttria-stabilized zirconia (YSZ) cermet anode, a dense YSZ electrolyte membrane, and a composite lanthanum strontium manganite (LSM)–YSZ cathode. In all cases the fuel is humidified H_2 and air is the oxidizer. The effects of porosity, tortuosity, and other microstructural geometric factors are evaluated with respect to their overpotential contributions. The model is used to assist interpretation of the experimental results reported by Zhao and Virkar [*J. Power Sources*, **141**, 79 (2005)]. The model results indicate that a correct formulation of concentration-gradients' dependence on tortuosity in porous electrodes provides a means for fitting the experimental data with reasonable support-layer tortuosity values (<5.0). Further, the fitting results indicate that there must be a physically reasonable negative correlation between support-layer porosity and tortuosity. The results also show that reducing anode porosity, which increases mass-transfer resistance, can significantly increase the thickness of the electrochemically active region. These results indicate the importance of incorporating detailed chemistry and distributed reaction zones to evaluate the design and performance of SOFC membrane electrode assemblies.
© 2008 The Electrochemical Society. [DOI: 10.1149/1.2898206] All rights reserved.

Although much solid oxide fuel cell (SOFC) research focuses on developing new high-performance materials, it is also known that electrode structure and microstructure significantly impact SOFC performance. It is well known that electrode functional layers and functionally graded architectures can be used to enhance SOFC performance.[1-3] Experiments by Zhao and Virkar[1] show that porosity in Ni–yttria-stabilized zirconia (YSZ) cermet anodes greatly influences performance, especially at high current densities. Recent studies by Barnett and others[4,5] have shown how barrier-layer architectures can be used to influence nonelectrochemical activity as well as overall electrochemical performance. Predictive models that quantitatively represent electrode microstructure can greatly benefit and accelerate the development of new high-performance electrode architectures.

The primary objective of this paper is to determine the interrelationships of electrode microstructural parameters that affect SOFC performance. Models of porous composite electrodes are usually formulated in terms of phenomenological parameters to characterize the porous-media structure.[5-9] These parameters include porosity ϕ_g, tortuosity τ_g, and specific catalyst area a_{cat} (i.e., area per unit volume) in both the electrochemically active and support layers. Although the parameters are often specified independently, results in this paper show that they are correlated.

The model reported in this paper advances the state-of-the-art in SOFC modeling. The model considers porous-media gas transport using the dusty-gas model (DGM) as well as parallel electron and ion transport via Ohm's law. The model extends efforts by some of the authors[8] by incorporating electrochemically active regions with nonzero thickness in both electrodes. While many past models have represented electrochemistry by single-step Butler–Volmer equations without reference to supporting surface chemistry on both the catalyst and electrolyte phases of the porous media electrodes, the model in this study incorporates heterogeneous surface chemistry and electrochemistry with elementary mass-action kinetics. This follows the recent approach for modeling electrochemistry in a study on patterned SOFC anodes[6] which was recently applied further to a multidimensional SOFC model with porous electrodes and a distributed electrochemistry model.[10] The current model largely follows the approach for heterogeneous chemistry/electrochemistry of this

recent study,[10] but this study differs significantly by implementing these approaches to fit model parameters for representing experimentally observed characteristics. This then provides a basis for evaluating how microstructural parameters influence, in particular, Ni–YSZ anode performance.

Zhao and Virkar report experimental button-cell performance using humidified H_2 over a wide range of Ni–YSZ anode support-layer porosities but with fixed structures for the anode functional layer, cathode, and electrolyte.[1] The present study uses these insightful experiments as a vehicle to validate models and to explore how microstructure parameters (principally ϕ_g and τ_g) are inter-related.

There are significant challenges in acquiring the data necessary to fully characterize the microstructure and performance of porous electrode architectures. Electrochemical polarization data, such as those reported by Zhao and Virkar, provide important measures of how electrode microstructure can influence cell performance. Performance measurements can be substantially augmented by direct microscopic observations. Among the important advances are three-dimensional tomographic reconstructions of electrode microstructure using dual-beam focused ion beam-scanning electron microscopy.[11] Although such mapping provides a detailed picture of electrode microstructure, practical SOFC computational models must still rely upon average phenomenological parameters to characterize porous-media transport and chemistry.

Model Formulation

The model is based on physical conservation laws that are derived as continuum partial-differential equations and then discretized with a finite-volume method and solved computationally. As illustrated in Fig. 1, the membrane electrode assembly (MEA) is composed of seven distinct elements: (*i*) fuel chamber, (*ii*) porous anode support layer (ASL), (*iii*) porous anode functional layer, (*iv*) dense electrolyte membrane, (*v*) porous cathode functional layer, (*vi*) porous cathode support layer, and (*vii*) air chamber.

The Ni–YSZ anode provides structural support with a relatively thick (1.0 mm here) ASL whose relatively high porosity provides low resistance to gaseous transport. Between the ASL and the dense electrolyte, a thin (20 μm in this study) Ni–YSZ functional layer has low porosity and high surface area to promote electrochemical reactions. There is a similarly thin (20 μm) functional layer for the lanthanum strontium manganite (LSM)–YSZ cathode, which has a relatively thin support layer (50 μm) that facilitates gaseous O_2 transport and current collection. The high specific catalyst area a_{cat} and high three-phase boundary length per unit volume l_{TPB} in the

* Electrochemical Society Student Member.
** Electrochemical Society Active Member.
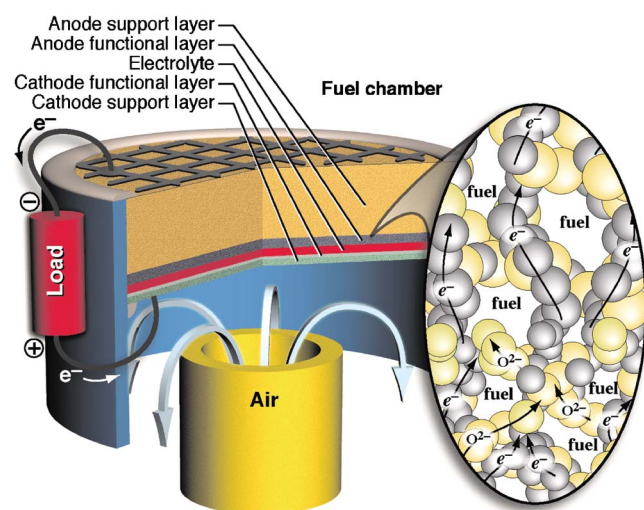z E-mail: gsjackso@umd.edu

Figure 1. (Color online) Layout of a typical button cell. The balloon illustrates ion and electron current paths near the interface between the anode support layer and anode functional layers. Particle sizes are typically smaller in the functional layer, where charge-transfer chemistry proceeds.

functional layers facilitate the surface and charge-transfer reactions necessary for electrochemical oxidation of the fuel in the anode or reduction of O_2 in the cathode.

In this study H_2 and H_2O are the only gases in the anode feed, and thus all nonequilibrated chemistry (including charge-transfer reactions) are confined to the electrode functional layers. Although thermal surface chemistry can occur throughout the electrode thickness, the high resistances associated with adsorbate surface diffusion and bulk ion transport significantly limit the spatial extent of the charge-transfer regions. Non-electrochemical surface chemistry, such as hydrocarbon-reforming or water-gas-shift processes, can occur in the support layers.[12] However, in the present study considering H_2 fuel and air oxidizer, the heterogeneous surface reactions outside of the electrochemically active region are in equilibrium under steady-state conditions and thus do not impact voltage–current relationships.

The governing conservation equations include the following physical phenomena for both the anode and the cathode: (*i*) convective and diffusive transport from the bulk gas chambers to the electrode surfaces, (*ii*) gas transport through porous electrode structures, described by DGM, (*iii*) reversible heterogeneous chemistry, including adsorption/desorption and charge-transfer reactions, and (*iv*) transport of O^{2-} ions in the electrolyte phase (YSZ) and electrons in the electrodes (Ni or LSM) as described by Ohm's law.

Gas-phase mass and species conservation.— Assuming ideal-gas behavior, the gaseous state is defined by two state variables (temperature T and mass density ρ) and the gas composition (represented by the mass fractions Y_k). The gas-phase species and overall mass-continuity equations are written as

$$\frac{\partial(\phi_g \rho Y_k)}{\partial t} + \frac{\partial j_k}{\partial y} = W_k a_{cat} \dot{s}_{k,cat} + W_k a_{elec} \dot{s}_{k,elec},$$

$$(K = 1, \dots K_{gas} - 1) \qquad [1]$$

$$\frac{\partial(\phi_g \rho)}{\partial t} + \sum_{k=1}^{K_{gas}} \frac{\partial j_k}{\partial y} = \sum_{k=1}^{K_{gas}} W_k(a_{cat}\dot{s}_{k,cat} + a_{elec}\dot{s}_{k,elec}) \qquad [2]$$

In these equations, j_k are the gas-phase mass fluxes, whose evaluation is discussed in a subsequent section. The molar production rates of gas-phase species by heterogeneous reactions on the catalyst and electrolyte surfaces are represented as $\dot{s}_{k,cat}$ and $\dot{s}_{k,elec}$, respectively. The specific areas (i.e., area per unit volume) available for catalytic

and electrochemical charge-transfer chemistry are a_{cat} and a_{elec}, respectively. The species molecular weights are W_k. The independent variables are time t and the spatial coordinate y. The species and overall continuity equations are not all independent. Thus, the species-continuity equations are applied for all but one of the species, and the remaining species mass fraction is evaluated as

$$Y_{K_{gas}} = 1 - \sum_{k=1}^{K_{gas}-1} Y_k \qquad [3]$$

Surface coverage.— On the catalyst surfaces and at the interfaces between the electrode and electrolyte phases, the surface coverages $\theta_{k,m}$ for species k on phase m (electrolyte or electrode) are represented as

$$\frac{\partial \theta_{k,m}}{\partial t} = \frac{1}{\Gamma_m}\left(\dot{s}_{k,m} + \frac{l_{TPB}}{a_m}\dot{s}_{k,m,TPB}\right) \qquad [4]$$

In this equation, Γ_m is the available surface sites per unit area, and $\dot{s}_{k,m}$ and $\dot{s}_{k,m,TPB}$ are surface production rates per unit area a_m and charge-transfer reaction rates per unit length of three-phase boundary l_{TPB}. In general, the reaction rates depend on local gas-phase state (i.e., temperature, density, and composition), surface-species coverages, and electric-potential differences between phases.

Charge conservation.— Assuming that all charge-transfer reactions take place within a finite volume adjacent to electrode–electrolyte interfaces, the charge balance in that volume must incorporate the sources and sinks due to the faradaic current i_{far} and the current densities due to electric-potential gradients. Equation 5 describes the conservation of charge in these electrochemically active regions as

$$C_{dl}\frac{\partial \Delta\Phi_{el}}{\partial t} \pm \frac{\partial}{\partial y}\left(\sigma_m^e \frac{\partial \Phi_m}{\partial y}\right) = l_{TPB} i_{far} \qquad [5]$$

The electric-potential difference between the electrode-phase (anode or cathode) electric potential $\Phi_{electrode}$ and the electrolyte-phase electric potential $\Phi_{electrolyte}$ is defined as $\Delta\Phi_{el} \equiv \Phi_{electrode} - \Phi_{electrolyte}$. The effective conductivity of phase m per unit of geometric area is σ_m^e. The double-layer capacitance per unit total volume C_{dl} can be extracted from equivalent-circuit modeling of experimental data.[13,14] The actual value of C_{dl} only impacts transient calculations and thus has no effect on the steady-state polarization curves reported herein. Thus, estimated values of C_{dl} are sufficient. The faradaic current density i_{far} (i.e., the local charge-transfer rate between phases at the three-phase boundaries) is calculated from the charge-transfer reaction rates $\dot{s}_{k,m,TPB}$. The $\pm$ sign on the left side of Eq. 5 depends on whether the particular phase in the composite electrode has a faradaic current that is producing or consuming electrons. Under steady-state conditions outside of the electrochemically active region, $i_{far} = 0$ and $i_{O^{2-}} = 0$, and hence $\partial\phi_{elec}/\partial y = 0$. Thus, the electric potential in the catalyst phase collapses to Ohm's law

$$i_{ext} = -\sigma_m^e \frac{\partial \Phi_m}{\partial y} \qquad [6]$$

Here, i_{ext} is the electronic (or ionic) current density (per geometric area) in the electrode (or electrolyte) phase. In the current study, σ_m^e for the porous electrode structures are calculated using a simple Bruggman correlation[3] where $\sigma_m^e = \phi_m^{3/2}\sigma_{m,bulk}$, ϕ_m is the volume fraction of conductive phase m, and $\sigma_{m,bulk}$ is the bulk conductivity of phase m. Integration of Eq. 5 in the electrochemically active region and the application of Eq. 6 throughout the rest of the electrode and electrolyte thicknesses determine the steady-state cell potential $V_{cell} = \Phi_{cathode,int} - \Phi_{anode,int}$, where the subscript int refers to the electrode interface with the fuel/air chamber.

The current study, like many previous SOFC modeling studies, assumes that equilibration time scales in the electrolyte are much faster than electrode processes. Thus, transient changes in local elec-

trolyte composition can be neglected. This places the restriction that the total charge-transfer currents at the two electrodes must be equal at any given time, which is always true for steady-state conditions. Thus, the voltage gradient across the dense-electrolyte membrane can be calculated from Ohm's law according to Eq. 6 for a given i_{ext}, where $\sigma_{electrolyte}^e = \sigma_{electrolyte,bulk}$, because the electrolyte is assumed to be fully dense and to be a pure ionic conductor.

Gas-phase transport.— Within porous electrodes, where the gas-phase mean-free-path length is often comparable with the average pore diameter, the effects of Knudsen diffusion and Darcy flow must be considered.[15] DGM is an implicit relationship among the gas-phase molar concentrations, concentration gradients, molar fluxes, and the pressure gradient.[15,16] As discussed in Zhu and Kee,[15] this relationship can be inverted to provide the gas-phase species mass flux j_k as

$$j_k = -W_k \left[\sum_l D_{kl}^{DGM} \frac{\partial [X_l]}{\partial y} + \sum_l D_{kl}^{DGM} \frac{[X_l]}{D_{l,Kn}^e} \frac{B_g}{\mu_g} \frac{\partial p}{\partial y} \right] \quad [7]$$

In this equation, $[X_l]$ is the molar concentration of species l, B_g is the permeability (evaluated according to the Cozeny–Karman relationship[15]), μ_g is the mixture dynamic viscosity, p is the pressure, and $D_{l,Kn}^e$ is the effective Knudsen diffusion coefficient for species l. As discussed in Zhu et al.,[15] the effective DGM diffusion coefficients are determined as a matrix inverse $D_{kl}^{DGM} = H^{-1}$, where the elements of the H matrix are

$$h_{kl} = \left[\frac{1}{D_{k,Kn}} + \sum_n \frac{X_n}{D_{kn}^e} + (\delta_{kl} - 1) \frac{X_k}{D_{kl}^e} \right] \quad [8]$$

The ordinary multicomponent diffusion coefficients D_{kn} are determined from the binary diffusion coefficients in the usual way.[17] The effective ordinary multicomponent diffusion coefficients are evaluated as

$$D_{kn}^e = \frac{\phi_g}{\tau_g} D_{kn} \quad [9]$$

The effective Knudsen diffusion coefficients are evaluated as

$$D_{k,Kn} = \frac{2}{3} \frac{\phi_g}{\tau_g} r_p \sqrt{\frac{8RT}{\pi W_k}} \quad [10]$$

where r_p is the pore radius. Note that both the ordinary and Knudsen diffusion coefficients are modified by the ratio ϕ_g/τ_g.

Equations 1 and 2 form a boundary-value problem whose solution requires boundary conditions at the interfaces with the dense-electrolyte and the bulk-gas compartments. Because the dense electrolyte is impervious to gas transport, $j_k = 0$ at the electrode–electrolyte interfaces. At the gas-compartment interfaces, the mass transfer is determined by considering a gas-phase mass-transfer boundary layer in the bulk gas. The flux-continuity at the interface is expressed as

$$j_{k,int} - Y_{k,int} \sum_l j_{l,int} = \frac{Sh_k D_{k,mix}}{L_{ch}} (\rho_{ch} Y_{k,ch} - \rho_{int} Y_{k,int}) \quad [11]$$

In this expression the subscript int indicates the interface and the subscript ch indicates the gas composition far from the interface. The mixture-averaged diffusion coefficient of species k with respect to the mixture composition in the gas compartment is $D_{k,mix}$. The Sherwood numbers Sh_k are related to the flow field, generally scaling with a Reynolds number. The characteristic length scale L_{ch} may be taken as the distance between an inlet tube (illustrated on the air side in Fig. 1) and the electrode interface. For the results shown in this paper the Sherwood numbers are fixed as $Sh_k = 3.5$. Because the resistance to gas transport in the bulk-gas boundary layer is small compared to the porous-media resistance, the results are found to be insensitive to the Sherwood number. Moreover, the interface composition is found to be nearly equal to the bulk-gas composition.

Surface and electrochemical reactions.— All surface reactions are simulated as reversible reactions, with rates calculated using the Cantera software package according to mass-action kinetics.[18] For reversible reactions, Cantera uses user-specified forward-reaction rate coefficients and thermodynamics to evaluate the reverse reaction rate coefficients.[17,19] For adsorption–desorption reactions, forward (adsorption)-rate coefficients are calculated as sticking coefficients

$$k_{fwd} = \frac{s^0}{\Gamma_m^\nu} \sqrt{\frac{RT}{2\pi W_k}} \quad [12]$$

where s^0 is the sticking probability and ν is the sum of the surface adsorbates' stoichiometric coefficients.[17] The forward-rate expressions for other surface reactions are described in Arrhenius form as

$$k^* = AT^\beta \exp\left(-\frac{E_a}{RT} \right) \quad [13]$$

As described by Bessler et al.,[6] the rate expressions for reactions involving charge transfer follow from mass-action kinetics as

$$k_{fwd} = k_{fwd}^* \exp\left(-\frac{\alpha_{fwd} n_{elec} F \Delta\Phi_{el}}{RT} \right) \quad [14]$$

$$k_{bwd} = k_{bwd}^* \exp\left(-\frac{\alpha_{bwd} n_{elec} F \Delta\Phi_{el}}{RT} \right) \quad [15]$$

The thermal component of the rate expressions, k_{fwd}^* and k_{bwd}^*, are expressed in Arrhenius form. The Faraday constant is F. The local electric potential difference between the electrode and electrolyte phases (Eq. 5) is represented as $\Delta\Phi_{el}$. The forward and backward symmetry parameters are α_{fwd} and α_{bwd}. In this study, the charge-transfer reaction rates follow the stipulation for elementary reactions that $\alpha_{fwd} + \alpha_{bwd} = 1$.[20] The number of electrons transferred in a reaction is given as n_{elec}.

The net rate of species production $\dot{s}_k$ depends upon summing the rate-of-progress q_i over all reactions

$$\dot{s}_k = \sum_{i=1}^I \nu_{kl} q_i \quad [16]$$

where $\nu_{ik} = \nu_{ik}'' - \nu_{ik}'$ is the stoichiometric coefficient of species k in reaction i. The reaction rate-of-progress is evaluated as

$$q_i = k_{i,fwd} \prod_{k=1}^K [X_k]^{\nu_{ki}'} - k_{i,bwd} \prod_{k=1}^K [X_k]^{\nu_{ki}''} \quad [17]$$

where ν_{ki}' is the stoichiometric coefficient of species k in the forward direction, ν_{ki}'' is the stoichiometric coefficient of species k in the backward direction, and $[X_k]$ is the generalized activity of the participating species. The activity of gas-phase species is the molar concentration, and the activity of surface species is the surface site density.[17] That is, for surface species

$$[X_k] = \frac{\theta_k \Gamma_m}{\zeta_k} \quad [18]$$

where Γ_m is the available site density (i.e., mol/m^2) on phase m and ζ_k is the number of sites occupied by species k. In the present study, each surface species occupies one site, $\zeta_k = 1$.

Thermodynamic consistency is necessary to ensure microscopic reversibility and hence to assure that $k_{i,fwd}$ and $k_{i,bwd}$ are consistent with the asymptotic approach to chemical equilibrium. In elementary electrochemistry, this consistency includes the prediction of open-circuit potential.[19] Most fuel-cell models incorporate the notion of an equilibrium Nernst potential, from which various overpotentials are subtracted. Here, however, when elementary charge-transfer chemistry is used, there is no need to evaluate the Nernst

Table I. Thermodynamics of species at 25 and 800°C.

	$h^0_{k,25°C}$ (kJ/g mol)	$s^0_{k,25°C}$ (J/g mol K)	$h^0_{k,800°C}$ (kJ/g mol)	$s^0_{k,800°C}$ (J/g mol K)
Gas-phase species				
O_2	0.0	204.3	25.3	245.0
H_2	0.0	131.5	22.9	168.4
H_2O	−241.2	190.4	−212.8	235.7
Ni surface species				
$[\ ]_{Ni}$	0.0	0.0	20.0	33.1
O_{Ni}	−237.7	18.8	−204.8	72.8
H_{Ni}	−40.4	28.6	−9.1	80.2
OH_{Ni}	−214.4	18.9	−173.8	85.1
$H2O_{Ni}$	−302.0	88.9	−253.5	167.3
YSZ bulk and surface species				
$[\ ]_{YSZ}$	0.0	0.0	47.8	78.9
O^{2-}_{YSZ}	−182.8	29.0	−122.3	128.9
$[\ ]_{YSZ(b)}$	0.0	0.0	47.8	78.9
$O^{2-}_{YSZ(b)}$	−182.8	29.1	−131.0	128.9
OH^-_{YSZ}	−245.7	47.7	47.8	165.9
H_2O_{YSZ}	−217.3	52.8	−293.4	177.0
LSM surface species				
$[\ ]_{LSM}$	0.0	0.0	32.2	53.2
O_{LSM}	−84.6	19.0	−39.5	93.2

Table III. Model parameters for the baseline cell.

	Anode	Cathode
TPB length, l_{TPB} (m^{-2})	3×10^{13}	3×10^{13}
Average pore radius, r_p (μm)	0.5	0.5
Average particle diameter, d_p (μm)	2.5	2.5
Utilization thickness, δ_{util} (μm)	5	5
Support-layer thickness (μm)	1000	50
Support-layer porosity (ϕ_g)	0.32	0.45
Support-layer tortuosity (τ_g)	3.5	2.9
Functional-layer thickness (μm)	20	20
Functional-layer porosity, $\phi_{g,int}$	0.23	0.26
Functional-layer tortuosity, $\tau_{g,int}$	4.5	4.5
Catalyst fraction of solid phase, ϕ_{cat}	0.6	0.5
Electrode site density, Γ_{cat} (mol/cm^2)	1.66×10^9	1.66×10^9
Electrode surface area, α_{cat} (m^{-1})	1×10^7	1×10^7
Electrolyte site density, Γ_{elec} (mol/cm^2)	1×10^9	1×10^9
Electrolyte surface area, α_{elec} (m^{-1})	1×10^7	1×10^7
Double-layer capacitance, C_{dl} (F/m^3)	0.003	0.2
Sherwood number, Sh	3.5	3.5

reactions on the YSZ surface are taken from Goodwin.[19] Finally, the kinetic rate parameters for O_2 reduction on an LSM–YSZ cathode are based on data reported by Jiang et al.[22] Table I provides thermodynamic properties for all species at 25 and 800°C. Table II lists all reactions and associated forward-rate parameters.

Simulation Procedure

Modeling an SOFC polarization curve requires a series of steady-state calculations for a range of specified current densities i_{ext}. In transient form and after finite-volume discretization of the spatial operators, the system of governing equations forms a system of differential-algebraic equations (DAEs). The DAE system is solved within the Matlab framework using the function ODE 15s. For each i_{ext} the solution is determined by solving the transient system to a steady state. For the baseline set of parameters, the simulation completed a sweep of 28 steady-state calculations, with $0 < i_{ext} < 2.5$ A/cm^2, in a time of 2.5 h on a 3.6 GHz processor.

Many physical and chemical parameters are needed to describe a particular MEA. Some parameters, such as physical dimensions, are easily established from the cell structure. Table III lists the parameters that are used to represent the performance of a baseline cell.

potential. Rather, predicting open-circuit potential (i.e., cell potential when there is no current flow) is the natural result of thermodynamic consistency.

In the present effort, thermodynamic properties and reaction-rate expressions are derived from a number of sources. As described by Bessler et al., forward and backward reaction rates are used to derive reaction thermodynamic parameters Δs^o_{rxn} and Δh^o_{rxn}, both of which are assumed constant.[6] Using the NASA polynomials as a set of reference thermodynamics for gas-phase species, and setting surface and bulk vacancies to arbitrary reference values, as described by Goodwin, reaction thermodynamic parameters are used to calculate the unknown thermodynamics for surface and bulk species.[19,21] For the nonelectrochemical reactions on the Ni anode catalyst, kinetic rate parameters are adopted from Janardhanan and Deutschmann.[8] The forward kinetic parameters and thermodynamics for charge-transfer reactions on a Ni–YSZ anode and for surface

Table II. Chemical and electrochemical reactions and forward rate expressions.

Reactions	A_{fwd} (g mol cm s)	β	$E_{act,fwd}$ (kJ/g mol)	α_{fwd}	Source
Ni surface					
$H_2 + 2[\ ]_{Ni} \rightleftharpoons 2H_{Ni}$	1.00×10^{-02a}	0	0		8
$O_2 + 2[\ ]_{Ni} \rightleftharpoons 2O_{Ni}$	1.00×10^{-02a}	0	0		8
$H_2O + [\ ]_{Ni} \rightleftharpoons H_2O_{Ni}$	1.00×10^{-01a}	0	0		8
$O_{Ni} + H_{Ni} \rightleftharpoons OH_{Ni} + [\ ]_{Ni}$	5.00×10^{22}	0	97.90		8
$H_2O_{Ni} + [\ ]_{Ni} \rightleftharpoons OH_{Ni} + H_{Ni}$	2.27×10^{21}	0	91.76		8
$2OH_{Ni} \rightleftharpoons O_{Ni} + H_2O_{Ni}$	3.00×10^{21}	0	100.00		8
Anode YSZ surface					
$H_2O + [\ ]_{YSZ} \rightleftharpoons H_2O_{YSZ}$	1.00×10^{a}	0	0		19
$O^{2-}_{YSZ(b)} + [\ ]_{YSZ} \rightleftharpoons [\ ]_{YSZ(b)} + O^{2-}_{YSZ}$	5.00×10^{07}	0	0		19
Ni–YSZ TPB					
$H_{Ni} + O^{2-}_{YSZ} \rightleftharpoons [\ ]_{Ni} + OH^-_{YSZ} + e^-_{Ni(b)}$	1.00×10^{16}	0	90.00	0.5	19
$H_{Ni} + OH^-_{YSZ} \rightleftharpoons H_2O_{YSZ} + e^-_{Ni(b)}$	1.00×10^{15}	0	90.00	0.5	19
LSM–YSZ TPB					
$O_{LSM} + [\ ]_{YSZ} + 2e^-_{LSM(b)} \rightleftharpoons O^{2-}_{YSZ} + [\ ]_{LSM}$	5.00×10^{17}	0	158.20	0.65	22
Cathode YSZ surface					
$O^{2-}_{YSZ(b)} + [\ ]_{YSZ} \rightleftharpoons [\ ]_{YSZ(b)} + O^{2-}_{YSZ}$	5.00×10^{07}	0	0		19
Cathode LSM surface					
$O_2 + 2[\ ]_{LSM} \rightleftharpoons 2O_{LSM}$	1.00×10^{-04a}	0	0		22

[a] Sticking coefficient, s^0.

The anode support layer is discretized into eight equal finite-volume cells, while the anode functional layer, cathode functional layer, and cathode support layer are discretized separately into four equal finite-volume cells.

In the active electrode functional layers, surface areas for the electrocatalyst and electrolyte, a_{cat} and a_{elec}, respectively, are estimated by assuming an average primary particle for each phase to be a 2.5 μm diameter hemisphere. This estimate provides a basis for specifying the values in Table III. The value for l_{TPB} per unit volume in Table III is estimated by assuming the 2.5 μm particles are well mixed. The final value for l_{TPB} is adjusted such that the low overpotential activation losses fit the experimental measurements of Zhao and Virkar.[1]

Another important parameter used in this simulation is derived from the concept of a "utilization region," which Adler discusses with regard to SOFC cathodes. This region is the thickness δ_{util} of the electrode in which ionic current is converted to electronic current by charge-transfer reactions (or vice versa, in the case of O_2 reduction in the cathode).[13] In the case of composite Pt–YSZ cathodes, Adler observes that δ_{util} can range from 0.4 to 20 μm, with typical values from 3 to 5 μm. The value of δ_{util} can be influenced by the thickness of a more-active functional layer, which explains why Zhao and Virkar observed reductions in overpotentials with increases in the cathode functional layer thickness up to 20 μm but not with increases beyond 20 μm.[1] Temperature and species composition can also influence δ_{util},[13] and thus it is not in general true that δ_{util} is equal to the thickness of the functional layer. Physically, any increase in δ_{util} provides additional l_{TPB}, a_{cat}, and a_{elec} for charge transfer and other key surface reactions but also results in an increase in the average path length through which O^{2-} ions must be transported. Although functional-layer microstructures are identical for all cells modeled here, δ_{util} may vary as a function of $\phi_{g,anode}$ due to its impact on gas-phase transport and H_2 concentration in the electrochemically active region.

For simulations in this study, δ_{util} is defined by the thickness of the finite volume adjacent to the dense electrolyte, because the non-equilibrium surface chemistry and electrochemistry are assumed to take place only in the finite volumes adjacent to the dense electrolyte. The specific value of δ_{util} is specified by discretizing the functional layer accordingly. For the baseline value of δ_{util} = 5 μm in Table III, the 20 μm functional layer is discretized into four finite volumes of equal thickness. Because the cathode microstructure is held fixed in this study, the $\delta_{util,cathode}$ in Table III remains constant for all simulations. For simulations with $\delta_{util,anode}$ less than the 5 μm baseline value, the functional layer is discretized into a coarser mesh. The current approach restricts δ_{util} to a user-defined parameter. Further modeling efforts will allow for nonequilibrium and electrochemistry to be distributed throughout all discretized finite volumes of the electrode functional and support layers, and such an approach will allow for δ_{util} to be calculated from the distributed electrochemistry calculations rather than specified by the user as in this current study. Nonetheless, the current study allows for δ_{util} variation to be studied parametrically to assess its variation with other electrode microstructure parameters.

Results

Zhao and Virkar reported experimental findings concerning the influence of electrode microstructure on button-cell performance.[1] They studied MEAs with varying anode support-layer porosity $\phi_{g,anode}$, anode support-layer thickness δ_{anode}, electrolyte thickness $\delta_{electrolyte}$, and cathode functional-layer thickness. Varying $\phi_{g,anode}$ is found to influence cell performance greatly. Thus, the present study focuses on determining the direct and indirect influences of $\phi_{g,anode}$ on polarization characteristics. Figure 2 (which is a reproduction of Zhao and Virkar's Fig. 9) shows the measured polarization characteristic for widely varying $\phi_{g,anode}$, with the characteristics of the anode functional layer held constant. These experiments were operated at T = 800°C and p = 1 atmosphere. The cathode was supplied
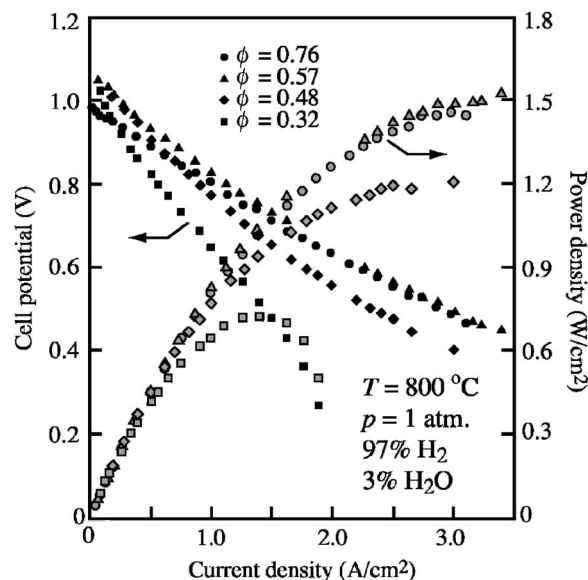

Figure 2. Experimental polarization and power-density measurements with varying anode porosity $\phi_{g,anode}$. (From Zhao and Virkar.[1])

with dry air and the anode with humidified hydrogen (i.e., 97% H_2 and 3% H_2O). The external current density i_{ext} was varied from 0 to 3.5 A/cm^2.

The anode support layer provides the majority of the MEA thickness for typical SOFC designs, and as such the effects of $\phi_{g,anode}$, $\tau_{g,anode}$, and other anode geometrical parameters can greatly impact mass transport and electrochemical performance. To isolate and explore the impact of these geometric parameters, this study focuses on anode-side microstructural variations while fixing the cathode-side parameters according to the baseline-cell conditions listed in Table III. In this sense, the present study follows the experimental exploration of Zhao and Virkar, who systematically varied ϕ_g in the anode support layer while holding all other parameters fixed, including those in the anode functional layers. However, as discussed below, other microstructural parameters, such as $\tau_{g,anode}$, may be covariant with $\phi_{g,anode}$.

Before beginning to model the experimental data of Fig. 2, $\phi_{g,anode}$ and $\tau_{g,anode}$ are varied independently from the baseline conditions to assess the sensitivity. Figure 3 shows the impact of varying $\phi_{g,anode}$ from 0.30 to 0.60, a range that is typical of practical MEA architectures.[1,23,24] As illustrated in Fig. 3, the simulation shows a relatively weak dependence on $\phi_{g,anode}$ alone. At low-to-moderate i_{ext} (i.e., < 1.5 A/cm^2), V_{cell} for the entire porosity range differs by less than 50 mV. For the lowest porosity ($\phi_{g,anode}$ = 0.30), gas diffusion becomes rate-limiting for i_{ext} > 1.5 A/cm^2, and there is a rapid increase in concentration overpotentials, resulting in V_{cell} dropping off quickly. However, $\phi_{g,anode}$ does not have a significant impact on the other polarization curves. By contrast, however, the experimental evidence in Fig. 2 shows that porosity has a significant impact on polarization. For the model to explain these data, there must be other significant parameter(s) of the anode microstructure that vary with $\phi_{g,anode}$.

One such covarying parameter is likely $\tau_{g,anode}$. Williford et al. reported experimentally determined $\tau_{g,anode}$ vs $\phi_{g,anode}$ for SOFC MEAs with Ni–YSZ cermet anodes using various measurement techniques.[24] Their results suggest two reasonable conclusions about $\tau_{g,anode}$: (*i*) $\tau_{g,anode}$ generally ranges from 2.0 to 4.5, and (*ii*) $\tau_{g,anode}$ decreases as $\phi_{g,anode}$ increases. The negative correlation between $\tau_{g,anode}$ and $\phi_{g,anode}$ makes intuitive sense, because removing solid particles to increase the void fraction should decrease the average path length of diffusing molecules.

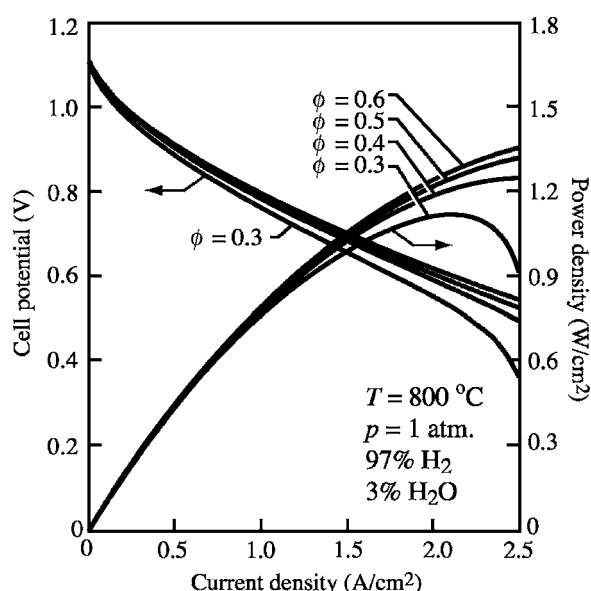Figure 4 shows the predicted effects of varying $\tau_{g,anode}$ while

Figure 3. Simulated polarization and power density with varying anode porosity but with all other parameters fixed at baseline values.
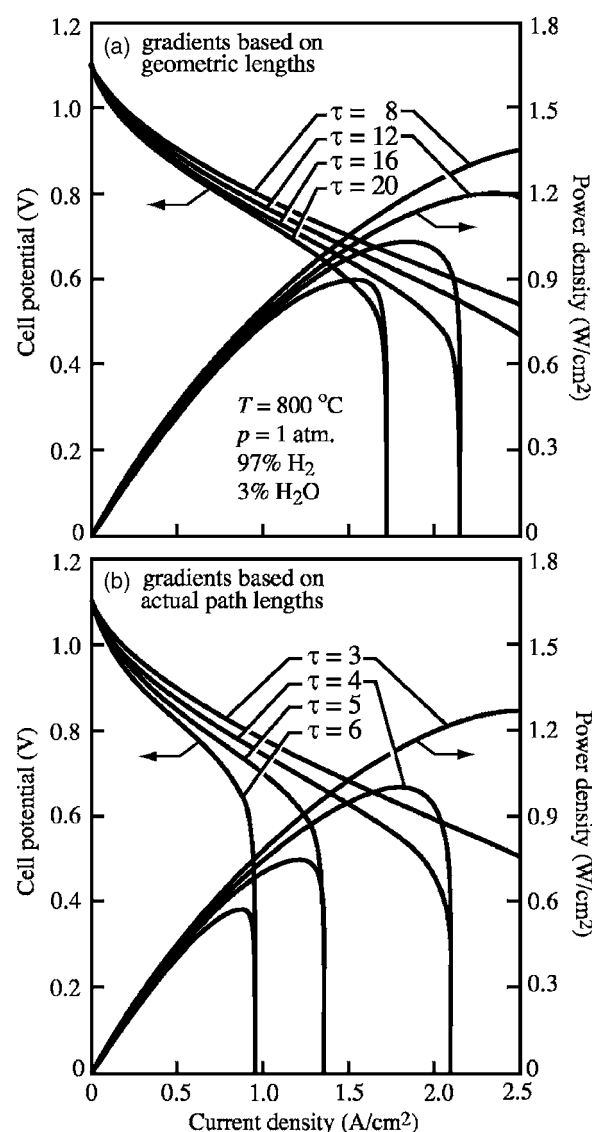

Figure 4. Simulated polarization and power density with varying anode tortuosity. The solutions in the upper panel are with gas-phase composition gradients computed using the physical coordinate. The solutions in the lower panel are with gas-phase composition gradients computed using the actual path lengths according to tortuosity.

holding all other parameters at their baseline condition. In Fig. 4a, property gradients in the diffusive transport equations are calculated according to the distance between the centers of adjacent finite volumes. Using this approach, high values of $\tau_{g,anode}$ (i.e., between 16 and 20) are needed to predict the measured transport-limited current densities below around 3 A/cm^2.[1] This supports the observations of Williford et al., who noted that models have required $\tau_{g,anode}$ as high as 17 to match experimental results with significant concentration polarization.[24] A number of different approaches have been reported to correct this discrepancy in SOFC modeling efforts.

1. Williford and Chick suggest that the anomalously high $\tau_{g,anode}$ are simply compensating for the absence of surface diffusion effects and propose a surface-diffusion mechanism based on the Vignes concept.[24]

2. A similar approach is advocated by O'Hayre et al., who describe a semiempirical method for modeling the impact of surface diffusion on the effective width of the triple-phase boundary (TPB).[25]

3. Zhu et al. use an effective $\phi_{g,anode}$ that is smaller (by approximately 35%) than the experimentally measured value.[12] They reason that the Kozeny–Carman relationship for the electrode permittivity is based on randomly packed spherical particles, while micrographs reveal that the sintered particles are clearly not spherical. Thus, their model uses $\phi_{g,anode} = 0.35$ to qualitatively match data from Jiang and Virkar[26] for an MEA with an experimentally determined $\phi_{g,anode} = 0.54$.

4. Haberman and Young derive a porous transport model in which the effective diffusion coefficients are $D^e = D\phi/\tau^2$.[27] In agreement with Haberman and Young, Epstein correctly points out that finite-difference approximations of local gradients of any diffusing property ψ in a porous media should employ the actual path length for the differencing distance $\tau\Delta y$.[28] In other words

$$\nabla\psi = \frac{\Delta\psi}{\Delta L} = \frac{\Delta\psi}{\tau\Delta y} \qquad [19]$$

where Δy is the distance between the centers of adjacent finite volumes. Epstein notes that this failure to distinguish between pore gradients and axial gradients was first done by Kozeny in 1927 and was explicitly corrected by Carman in 1956. Nevertheless, the initial error has been propagated by numerous researchers.[28]

Each of the above approaches has merit and is attempted in the current study. Surface-diffusion effects may certainly be significant

at high i_{ext}.[24] However, this approach is not attempted here due to the high degree of uncertainty in physical models of surface diffusion and magnitude of diffusion coefficients. It is expected that development and inclusion of surface-diffusion models will improve modeling capabilities, but it is unclear how the competition between surface diffusion and adsorption–desorption near the TPB impacts the need for such improved surface-diffusion models.

Of all the approaches mentioned above, the use of Eq. 19 to evaluate diffusive gradients in the porous matrix provides the most effective means to match experimental data using tortuosities $\tau_{g,anode}$ that are within the range of measured values for Ni–YSZ anodes.[24] Figure 4b shows the effect of $\tau_{g,anode}$ when gradients are evaluated using Eq. 19. While evaluating gradients using the physical coordinates (i.e., Fig. 4a) requires $\tau_{g,anode} = 16$ to predict reasonable limiting current density, the corrected porous-media gradients require $\tau_{g,anode} = 4$ to achieve experimentally observed current densities. Thus, it appears likely that the method for evaluating gradients is responsible for unusually high tortuosities that have been in some earlier models to predict the effects of concentration polarization.
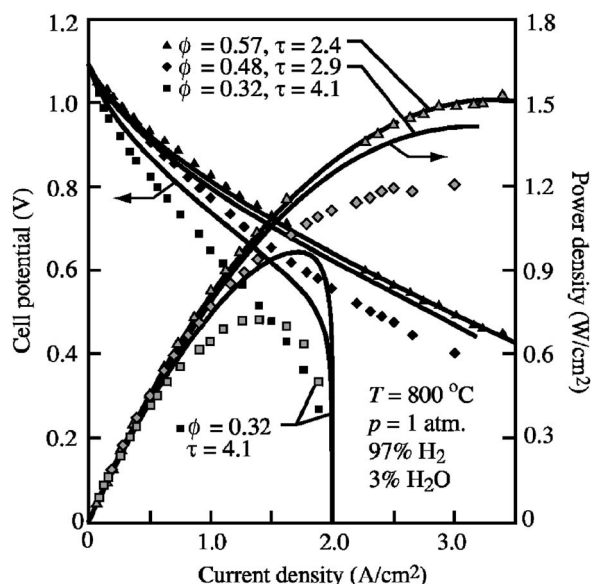
Figure 5. Simulated polarization and power density with covarying anode porosity and tortuosity. Symbols are experimental data from Zhao and Virkar.[1] The utilization thickness is fixed at 5 μm for all cases.
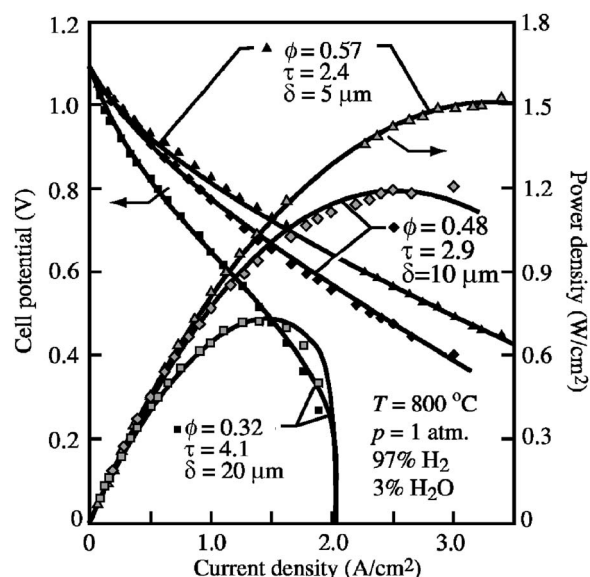

Figure 6. Simulated polarization and power density with covarying anode porosity, tortuosity, and utilization thickness. Symbols are experimental data from Zhao and Virkar.[1]

As discussed earlier, a negative correlation between $\tau_{g,anode}$ and $\phi_{g,anode}$ in porous SOFC electrodes should be expected. Therefore, it is interesting to covary these two parameters in predicting the influence of porosity on cell performance. Figure 5 shows the polarization curves for specific combinations of $\tau_{g,anode}$ and $\phi_{g,anode}$. Model results are shown for the values of $\phi_{g,anode}$ used in the Zhao and Virkar experiments[1] and are compared to the experimental measurements. The tortuosity $\tau_{g,anode}$ increases from 2.4 to 4.1 as $\phi_{g,anode}$ decreases from 0.57 to 0.32 in order for the model to give reasonable agreement with the experimental data. The experiments for $\phi_g = 0.76$ are not modeled here because, as Zhao and Virkar note, that particular cell suffered from leakage current.

Figure 5 shows that the simulations for $\phi_{g,anode} = 0.57$ agree well with the experimental data. The model also correctly predicts the limiting current density for $\phi_{g,anode} = 0.32$. Nevertheless, there are significant discrepancies between the experimental and simulated results. Most noticeably, the curves for $\phi_{g,anode} = 0.32$ and 0.48 significantly underpredict the overpotentials for all current densities. Thus, while the limiting current density for $\phi_{g,anode} = 0.32$ is essentially correct, the maximum power density for this cell is predicted to be 0.97 W/cm², while the measured value is 0.71 W/cm². Despite capturing some aspects of the measured polarization, it is evident from Fig. 5 that this combination of $\phi_{g,anode}$ and $\tau_{g,anode}$ provides a poor overall representation of the data. For example, at 1.5 A/cm², comparing the cell potentials for $\phi_{g,anode} = 0.32$ and $\phi_{g,anode} = 0.57$ shows a difference of only 170 mV, while Fig. 2 shows a difference of about 240 mV. Attempts to further manipulate $\tau_{g,anode}$ to fit the experimental data would force it to values outside reasonable ranges. This would involve either decreasing the tortuosity for $\phi_{g,anode} = 0.57$ or increasing the tortuosity for $\phi_{g,anode} = 0.32$. The former would likely lead to disagreement between the model and experiment at higher current densities, while the latter would cause a discrepancy between the observed and predicted limiting current densities. Because of this, it may be hypothesized that yet another parameter may covary with $\phi_{g,anode}$ and $\tau_{g,anode}$.

The utilization thickness parameter $\delta_{util,anode}$ tends to vary with changes in $\phi_{g,anode}$. Changes in $\delta_{util,anode}$ are derived from changes in mass-transport resistance impacting diffusion rates and thus surface activity within the anode functional layer. Figure 6 shows the polarization and power density curves with covarying $\phi_{g,anode}$, $\tau_{g,anode}$, and $\delta_{util,anode}$ with the intent of comparing the modeling results with

the experimental data from Fig. 2. Figure 6 shows that the model results agree with the experiments by allowing $\delta_{util,anode}$ to increase with decreasing $\phi_{g,anode}$. The cell with $\phi_{g,anode} = 0.57$ has the least resistance to gas-phase diffusion and thus the highest p_{H_2} in the electrochemically active region for a given current density (at $i_{ext} = 2$ A/cm², the model predicts $p_{H_2} = 0.768$ atmosphere in the electrochemically active region near the electrolyte interface). Higher p_{H_2} increases charge-transfer reaction rates and thereby reduces the distance (i.e., $\delta_{util,anode}$) required for O^{2-} conduction from the electrolyte into the porous anode functional layer. For this high $\phi_{g,anode}$, a reasonable value of $\delta_{util,anode} = 5$ μm provided a good match to the experimental data.

Decreasing porosity $\phi_{g,anode}$ increases gas-phase diffusion resistance, which reduces p_{H_2} in the electrochemically active region. For example, at $i_{ext} = 2$ A/cm², the model used for Fig. 6 predicts $p_{H_2} = 0.651$ and 0.031 atmosphere for $\phi_{g,anode} = 0.48$ and 0.32, respectively. Reducing H_2 concentration reduces local charge-transfer rates and thus suggests the need for increasing $\delta_{util,anode}$ to support high current densities. As noted elsewhere,[6] the decrease in p_{H_2} has a thermodynamic effect on Butler–Volmer kinetics, which increases the activation overpotentials (i.e., the charge-transfer polarization resistance). In light of this reasoning, it is not surprising that for the model to predict the experimental data in Fig. 6, $\delta_{util,anode}$ increases to 10 and 20 μm for the cells with $\phi_{g,anode}$ of 0.48 and 0.32, respectively.

As a means of comparing the implementation of the DGM used in this study to previous modeling efforts, Fig. 7 shows species and pressure profiles through the anode thickness for current densities of 0.5, 1.5, and 2.5 A/cm². As expected for the binary H_2–H_2O system, the profiles are linear. However, within the 20 μm functional layer (which has lower porosity) the gradients are significantly higher than in the support layer. The magnitudes of all gradients increase as the current density increases. Table IV summarizes the predicted gradients in the anode support layer for the solutions illustrated in Fig. 7. While it is difficult to make direct comparisons between different modeling efforts, given the large number of parameters involved, the nominal pressure and concentration gradients should be comparable. Zhao and Virkar present a parametric modeling study of their experimental observations.[1] Lehnert et al.[29] and Gemmen and Trembley[7] model SOFCs operating on reformed methane
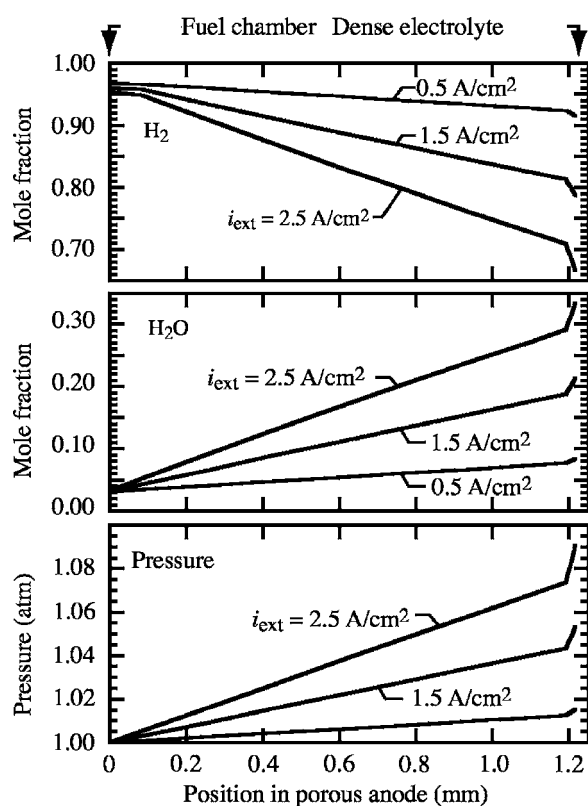
Figure 7. Hydrogen, steam, and pressure profiles through the porous anode thickness at selected current densities. In all cases, $\phi_{g,anode} = 0.57$, $\tau_{g,anode} = 2.4$, and $\delta_{until,anode} = 5$ μm.

but with operating conditions similar to the present investigation. The results of the present study are consistent with previous investigations.

Discussion

This study reveals the importance of considering physical correlations among several microstructural parameters that describe porous electrodes. The results also emphasize the importance of considering the full range of current densities (i_{ext}) when determining the microstructural parameters that best represent cell polarization characteristics. The present study focuses especially on physical porous-media characteristics without exploring other uncertain characteristics such as surface thermodynamics and chemical kinetics. Rather, as summarized in Tables I and II, these parameters are based on previous literature. Nevertheless, from the model studies presented here, it is clear that reasonable variation of those parameters would not provide adequate sensitivity to match the rapid fall-off in the polarization characteristics near the limiting current densities (which vary greatly with $\phi_{g,anode}$). Because at low i_{ext} activation overpotentials dominate relative to concentration overpotentials, it is possible to predict polarization behavior at low current density even with significant errors in the mass-transport model parameters.[24] Polarization behavior at high current density provides a more rigorous

Table IV. Pressure and concentration gradients in the anode support layer with $\phi_{g,anode} = 0.57$.

i_{ext} (A/cm^2)	$\partial p/\partial y$ (atm/m)	$\partial[H_2]/\partial y$ (kmol/m^4)	$\partial[H_2O]/\partial y$ (kmol/m^4)
0.5	1.26	−0.35	0.51
1.5	4.41	−1.23	1.80
2.5	7.52	−2.11	3.09

Table V. Comparison of R_{ohm} values from experiment and simulations for varying anode microstructures.

	R_{ohm} (Ω cm^2)	
$\phi_{g,anode}$	Zhao and Virkar[1]	This work
0.32	0.90	0.079
0.48	0.104	0.113
0.57	0.156	0.182

test of mass-transport models and fits for the microstructure parameters, such as $\phi_{g,anode}$ and $\tau_{g,anode}$, that significantly impact transport.

Although much can be learned from model-based interpretation of polarization characteristics, the approach provides only indirect measures of the controlling microstructural characteristics. Because porous-media transport is important to cell performance, especially at high current density, it is important to find independent measures of the critical parameters. Three-dimensional tomographical reconstruction of electrode materials provides an important, direct route to establish needed microstructural parameters.[11]

One means of evaluating fitting parameters is to predict how bulk resistance R_{bulk} varies with $\phi_{g,anode}$. Because R_{bulk} depends almost exclusively on the resistance to O^{2-} ion current in the electrolyte phase, its value increases (or decreases) with $\delta_{util,anode}$ due to the increase (or decrease) with average distance of travel of O^{2-} ions into the anode functional layer. As shown in Table V, the calculated R_{bulk} from this study for the varying $\delta_{util,anode}$ used in Fig. 6 compares favorably with the variation in R_{bulk} measured by Zhao and Virkar.[1] The significant variation in R_{bulk} illustrates the importance of the functional layer and the associated $\delta_{util,anode}$ in determining the net bulk resistance. Furthermore, because $\delta_{util,anode}$ can also depend on reactant partial pressures, R_{bulk} itself may also vary significantly with fuel partial pressures. Finally, the agreement between experimental and simulation R_{bulk} values removes much of the uncertainty surrounding the absolute values of $\delta_{util,anode}$ and $l_{TPB,anode}$. While the values of $l_{TPB,anode}$, as mentioned, were tuned to fit the low-polarization characteristics of the experimental data, this fitting was performed with an arbitrarily assumed value of $\delta_{util,anode} = 5$ μm. Because the total TPB length for an electrode depends on the product of l_{TPB} and δ_{util}, a different assumption for $\delta_{util,anode}$ would affect the fitting of the $l_{TPB,anode}$ variable. The modest agreement between R_{bulk} values, however, lends validity to the absolute values of $\delta_{util,anode}$ used in this simulation as well as the overall magnitude of $l_{TPB,anode}$.

The current model shows the importance of assessing the extent of the electrochemically active region $\delta_{util,anode}$ within the electrode structure. Variation in $\delta_{util,anode}$ for alternative MEA architectures suggests the importance of establishing l_{TPB}, a_{cat}, and a_{elec} as functions of functional-layer microstructure. These parameters are derived from the variation in depth of the active region. The current model allows $\delta_{util,anode}$ to be a fitting parameter. However, $\delta_{util,anode}$ should be established from a more rigorous approach that allows for electrochemistry to occur throughout the depth of the electrode (including beyond the functional layer). Such an approach has been implemented in past models which modeled the electrochemistry as a single-step Butler–Volmer reaction and as such did not capture the complex supporting surface chemistry on both the catalyst and electrolyte phases.[30-34] Distributed electrochemically active regions using the elementary kinetic models presented here have been performed as extensions of the present study. However, they are not reported in this paper. These models show that $\delta_{util,anode}$ varies with p_{H_2} and thus with increases in i_{ext}. Such variation with i_{ext} is not captured in this study because $\delta_{util,anode}$ is fixed for a particular MEA microstructure. Nevertheless, because the impact of the additional ohmic overpotentials with the higher $\delta_{util,anode}$ is minor at lower i_{ext}, the fitted $\delta_{util,anode}$ primarily improve the fits in Fig. 6 for the high

i_{ext}. Nonetheless, models with the capability to predict distributed electrochemistry throughout the cell will enhance quantitative predictive capability.

It is important to re-emphasize that this study is not intended to provide exact measures of the fitted parameters; rather, the model is used to explore the effect of several microstructural parameters and their likely inter-relationships. The inclusion of surface diffusion may improve the model, but more work is needed to measure (or estimate) surface diffusivities and length scales before these models can be effective.[24] Modeling patterned-anode experiments with well-defined geometries is likely to prove helpful in the development of surface-diffusion and charge-transfer models and thus contribute to improving MEA models.[6,19]

Conclusions

The comparison of model predictions and experimental data of Zhao and Virkar[1] provides the basis for assessing how key microstructural parameters in porous Ni–YSZ anodes are inter-related. Predicting the experimental observations requires physically reasonable correlations between $\phi_{g,anode}$, $\tau_{g,anode}$, and $\delta_{util,anode}$. These correlations enabled the accurate prediction of button-cell polarization characteristics using physical parameters whose values are consistent with independent measurements. Values of tortuosity $\tau_{g,anode}$ between 2 and 5 are facilitated by correcting the transport-gradient calculations according to Epstein.[28] The models show the importance of porous-electrode microstructural characteristics on cell performance. Thus, to assist continuing development of model-based cell design and optimization, it is important to establish underpinning functional relationships and needed physical parameters. In addition to modeling polarization behavior, as done in the present paper, experiments such as patterned electrodes and tomographic reconstructions can play a valuable role in the independent measurement of critical functional relationships and physical parameters.

Acknowledgments

References

1. F. Zhao and A. V. Virkar, *J. Power Sources*, **141**, 79 (2005).
2. A. Weber and E. Ivers-Tiffée, *J. Power Sources*, **127**, 273 (2004).
3. B. Kenney and K. Karan, *Solid State Ionics*, **178**, 297 (2007).
4. Y. B. Lin, Z. L. Zhan, and S. A. Barnett, *J. Power Sources*, **158**, 1313 (2006).
5. H. Zhu, A. M. Colclasure, R. J. Kee, Y. B. Lin, and S. A. Barnett, *J. Power Sources*, **161**, 413 (2006).
6. W. G. Bessler, J. Warnatz, and D. G. Goodwin, *Solid State Ionics*, **177**, 3371 (2007).
7. R. S. Gemmen and J. Trembly, *J. Power Sources*, **161**, 1084 (2006).
8. V. M. Janardhanan and O. Deutschmann, *J. Power Sources*, **162**, 1192 (2006).
9. H. Zhu and R. J. Kee, *J. Electrochem. Soc.*, **153**, A1765 (2006).
10. W. G. Bessler, S. Gewies, and M. Vogler, *Electrochim. Acta*, **53**, 1782 (2007).
11. J. R. Wilson, W. Kobsiriphat, R. Mendoza, H. Y. Chen, J. M. Hiller, D. J. Miller, K. Thornton, P. W. Voorhees, S. B. Adler, and S. A. Barnett, *Nat. Mater.*, **5**, 541 (2006).
12. H. Zhu, R. J. Kee, A. V. Janardhanan, O. Deutschmann, and D. G. Goodwin, *J. Electrochem. Soc.*, **152**, A2427 (2005).
13. S. B. Adler, *Chem. Rev. (Washington, D.C.)*, **104**, 4791 (2004).
14. A. Mitterdorfer and L. J. Gauckler, *Solid State Ionics*, **117**, 203 (1999).
15. H. Zhu and R. J. Kee, *J. Power Sources*, **117**, 61 (2003).
16. M. Kaviany, *Principles of Heat Transfer in Porous Media*, Springer, New York (1995).
17. R. J. Kee, M. E. Coltrin, and P. Glarborg, *Chemically Reacting Flow: Theory and Practice*, John Wiley & Sons, Hoboken, NJ (2003).
18. D. G. Goodwin, in *Chemical Vapor Deposition XVI and EUROCVD 14*, M. Allendorf, F. Maury, and F. Teyssandier, Editors, PV 2003-08, pp. 155–162, The Electrochemical Society Proceedings Series, Pennington, NJ (2003), see also http://www.cantera.org
19. D. G. Goodwin, *Solid Oxide Fuel Cells IX*, S. Singhal and J. Mizusaki, Editors, PV 2005-7, pp. 699–707, The Electrochemical Society Proceedings Series, Pennington, NJ, (2005).
20. A. J. Bard and L. R. Falkner, *Electrochemical Methods; Fundamentals and Applications*, John Wiley & Sons, New York (1980).
21. S. Gordon and B. J. McBride, NASA reference publication 1311, Houston, TX (1994).
22. Y. Jiang, S. Z. Wang, Y. H. Zhang, J. W. Yan, and W. Z. Li, *Solid State Ionics*, **110**, 111 (1998).
23. T. S. Lai and S. A. Barnett, *J. Power Sources*, **147**, 85 (2005).
24. R. E. Williford, L. A. Chick, G. D. Maupin, S. P. Simner, and J. W. Stevenson, *J. Electrochem. Soc.*, **150**, A1067 (2003).
25. R. O'Hayre, D. M. Barnett, and F. B. Prinz, *J. Electrochem. Soc.*, **152**, A439 (2005).
26. Y. Jiang and A. V. Virkar, *J. Electrochem. Soc.*, **150**, A942 (2003).
27. B. A. Haberman and J. B. Young, *J. Fuel Cell Sci. Technol.*, **3**, 312 (2006).
28. N. Epstein, *Chem. Eng. Sci.*, **44**, 777 (1989).
29. W. Lehnert, J. Meusinger, and F. Thom, *J. Power Sources*, **87**, 57 (2000).
30. T. Kenjo, S. Osawa, and K. Fujikawa, *J. Electrochem. Soc.*, **138**, 349 (1991).
31. C. W. Tanner, K. Z. Fung, and A. V. Virkar, *J. Electrochem. Soc.*, **144**, 21 (1997).
32. P. Costamagna, P. Costa, and V. Antonucci, *Electrochim. Acta*, **43**, 375 (1998).
33. J. Divisek, R. Jung, and I. C. Vinke, *J. Appl. Electrochem.*, **29**, 165 (1999).
34. S. H. Chan and Z. T. Xia, *J. Electrochem. Soc.*, **148**, A388 (2001).